Absorption-Based Hyperspectral Thermal Ranging: Performance Analyses, Optimization, and Simulations

UNAY DORKEN GALLASTEGI,[1,*] HOOVER RUEDA-CHACÓN,[2] MARTIN J. STEVENS,[3] AND VIVEK K GOYAL[1]

[1]*Department of Electrical and Computer Engineering, Boston University, Boston, MA, 02215, USA*
[2]*Department of Computer Science, Universidad Industrial de Santander, Bucaramanga, 680002, Colombia.*
[3]*National Institute of Standards and Technology, Boulder, CO, 80305, USA*
[*]*udorken@bu.edu*

Abstract: The wavelength dependence of atmospheric absorption creates range cues in hyperspectral measurements that can be exploited for passive ranging using only thermal emissions. In this work, we present fundamental limits on absorption-based ranging under a model of known air temperature and wavelength-dependent attenuation coefficient, with object temperature and emissivity unknown; reflected solar and environmental radiance is omitted from our analysis. Fisher information computations illustrate how performance limits depend on atmospheric conditions such as air temperature and humidity; temperature contrast in the scene; spectral resolution of measurement; and distance. These results should prove valuable in sensor system design.

1. Introduction

It is well known that thermal radiation is ubiquitous since all bodies in nature emit energy. It is less known that thermal radiation can be used for range estimation. As thermal radiation propagates, attenuation by atmospheric absorption is by an amount dependent on wavelength and distance traveled, and this has been exploited for passive ranging [1–7]. Whereas typical passive ranging based on stereo has performance that degrades sharply with increasing distance and decreasing scene texture, absorption-based ranging does not depend on scene texture and has performance that may decay more slowly with increasing distance. Furthermore, with fine spectral resolution, the influence of emissivity can be separated from atmospheric attenuation to enable object material identification. By operating in the long-wave infrared (LWIR) range, this technology can work in daylight and pitch dark since it does not rely on active external light sources or sunlight.

Whereas most initial developments of absorption-based ranging were for objects significantly hotter than the air, ranging for natural scenes with typical temperature contrast of around 4 K [8] is a more challenging problem. Our previous work [9, 10] shows methods that use two or more spectral channels to recover range, emissivity and temperature for static natural scenes. For that work, the LWIR measurements were acquired using the best available instruments, which required long integration times and were limited to a specific spectral range.

In this paper, we address the shot noise-limited sensing model that is appropriate for low photon count regimes. This is particularly applicable for short integration times, such as when fast inference is required for autonomous navigation. In contrast to other single-photon detectors, superconducting nanowire single-photon detectors (SNSPDs) are sensitive to a wide range of the spectrum, making them suitable for absorption-based ranging by spanning many absorption lines in the spectrum. Inspired by the potential availability of shot noise-limited single-photon detection at any desired wavelengths, we aim to understand the ultimate limits of absorption-based ranging and how to design a sensor that could fully exploit this technique.

In Section 2, we discuss the radiative transfer and sensing model that we analyze. In Section 3,

we derive the Fisher information and Cramér-Rao bound (CRB) for ranging under a spline model for the emissivity. This model creates spectrally smooth approximate emissivities and reduces the number of parameters to avoid an underdetermined inverse problem. In Section 4, we present an estimator using an approximate likelihood designed for shot noise, using the spline model. In Section 5, we analyze the tradespace of the problem using Fisher information in the infrared spectrum from 4 µm to 20 µm, and we evaluate the CRB under different sensor parameters such as pixel size, solid angle, integration time, and channel resolution. We also examine the influence of read noise on our performance limits.

2. Emission, Atmospheric Absorption, and Sensing Model

Assuming thermal equilibrium, observed radiance can be expressed using a well-established atmospheric absorption and emission model [11]. Although most scenes are not strictly at thermal equilibrium, this assumption yields good approximations when thermal contrast is low [12]. In this model, the radiance observed at the sensor, $L_{\text{obs}}(\lambda)$, is the sum of two terms: the object emission $L_{\text{obj}}(\lambda)$ and the air emission $L_{\text{air}}(\lambda)$, where λ represents the wavelength.

An object with temperature T_{obj} and emissivity profile $\varepsilon(\lambda)$ emits a radiance $\varepsilon(\lambda)B(\lambda; T_{\text{obj}})$, where $B(\,\cdot\,;\cdot\,)$ is the black-body radiation. As the radiance propagates through the atmosphere to the sensor, it is attenuated due to atmospheric absorption. The radiance reaching the sensor is thus given by

$$L_{\text{obj}}(\lambda) = \tau(\lambda)\varepsilon(\lambda)B(\lambda; T_{\text{obj}}), \tag{1}$$

where $\tau(\lambda)$ is the wavelength-dependent atmospheric transmittance function that represents the fraction of radiance not lost due to absorption. We assume thermal equilibrium and no scattering; therefore it follows from Kirchhoff's law of thermal radiation that the air emissivity is $1 - \tau(\lambda)$. The radiance reaching the sensor from air with temperature T_{air} is thus given by

$$L_{\text{air}}(\lambda) = (1 - \tau(\lambda))B(\lambda; T_{\text{air}}). \tag{2}$$

Following Beer's law, the atmospheric transmittance $\tau(\lambda)$ can be expressed as

$$\tau(\lambda) = 10^{-\alpha(\lambda)d/10}, \tag{3}$$

where $\alpha(\lambda)$ is the wavelength-dependent attenuation coefficient, in units of dB/m, and d is the range (between the object and the sensor), in units of meters (m). The attenuation profile is specific to atmospheric parameters such as gas concentration, pressure, and air temperature; a detailed explanation and some representative atmospheric models are provided in Section 5.1.

By adding Eq. (1) and Eq. (2) and substituting Eq. (3), the observed radiance in the sensor can be written as

$$\begin{aligned} L_{\text{obs}}(\lambda) &= L_{\text{obj}}(\lambda) + L_{\text{air}}(\lambda) \\ &= 10^{-\alpha(\lambda)d/10}(\varepsilon(\lambda)B(\lambda; T_{\text{obj}}) - B(\lambda; T_{\text{air}})) + B(\lambda; T_{\text{air}}), \end{aligned} \tag{4}$$

where the black-body radiation is

$$B(\lambda; T) = \frac{2 \times 10^{-4} hc^2}{\lambda^5} \frac{1}{e^{hc/\lambda k_{\text{B}} T} - 1} \tag{5}$$

in units of microflicks ($\mu\text{W} \cdot \text{sr}^{-1} \cdot \text{cm}^{-2} \cdot \mu\text{m}^{-1}$), where h is the Planck constant and c is the speed of light.

For calculations, we discretize the model Eq. (4) finely in wavelength using a sampling interval $\Delta_\lambda = 0.0198$ nm. This is fine enough to including a few samples per absorption line; atmospheric gasses under typical conditions exhibit absorption lines with widths of approximately 1 nm at

short wavelengths ($\approx 4\,\mu$m) and 10 nm at long wavelengths ($\approx 17\,\mu$m) [13]. The fine resolution allows us to use Beer's law and avoid the more complicated form of mean absorption across wider bands [14]. Then we define photon rate vectors for narrow bands with width Δ_λ as $\mathbf{b} \in \mathbb{R}^N$ and $\boldsymbol{\ell} \in \mathbb{R}^N$, where N is the number of samples in the spectrum,

$$\begin{aligned} b_i(T) &= \frac{\lambda_i}{hc}\Delta_\lambda B(\lambda_i; T), \\ \ell_i &= 10^{-\alpha_i d/10}(\varepsilon_i b_i(T_{\text{obj}}) - b_i(T_{\text{air}})) + b_i(T_{\text{air}}), \end{aligned} \tag{6}$$

in photon rates (photon $\cdot\, \text{s}^{-1}\cdot\text{sr}^{-1}\cdot\text{cm}^{-2}$). The spectral resolution of measurement will generally be much coarser, with K spectral measurements, $K \ll N$. The mean photon count vector $\boldsymbol{\nu} \in \mathbb{R}^K$ depends on the sensor parameters, including quantum efficiency η_k, pixel area A (cm^2), solid angle Ω (sr), integration time t_d (s), and channel resolution $\Delta\lambda$ (nm). The mean photon count in spectral channel k is

$$\nu_k = \rho_k \sum_{i=c_k^l}^{c_k^u} \ell_i, \tag{7}$$

where $\rho_k = \eta_k A \Omega t_d$ is a scale factor and c_k^l and c_k^u represent the lower and upper indices of the channel dictated by the channel resolution. In this work, we assume a uniform detector efficiency and hence that $\rho_k = \rho$, with no band dependence. For a chosen channel resolution $\Delta\lambda$, the indices are $c_k^l = (k-1)\lfloor \Delta\lambda/\Delta_\lambda \rceil + 1$ and $c_k^u = k\lfloor \Delta\lambda/\Delta_\lambda \rceil$, and the number of measurements is $K = \lceil N/\lfloor \Delta\lambda/\Delta_\lambda \rceil \rceil$, where $\lfloor\cdot\rceil$ indicates rounding to the nearest integer, and $\lceil\cdot\rceil$ is the ceiling operator. For shot noise-limited sensors, the read noise can be ignored, and the elements of the measurement vector $\mathbf{y} \in \mathbb{R}^K$ can be modeled as independent random variables following Poisson distribution as

$$y_k \sim \text{Poisson}(\nu_k). \tag{8}$$

In this model, we assume that the reflected environmental radiance is negligible. This is appropriate for high-emissivity objects since the emissivity and reflectance sum to 1. However, in the case of low-emissivity objects, it is crucial to consider the contribution of reflected environmental radiance to prevent model mismatch. In [9], we showed that the reflected sky radiance can lead to distance overestimation, as spectra of sky radiance and transmittance exhibit shared absorption lines.

3. Fisher Information and Cramér-Rao Bound

The Cramér-Rao Bound (CRB), defined as the inverse of the Fisher information (FI), gives a lower bound on the variance of an unbiased range estimate. First, we derive the FI for each spectral channel assuming that only the range is unknown. Then, unknown parameters from object emission (emissivity and temperature) are included in the analysis.

Based on the shot-noise model in Eq. (8), the FI in observation y_k for the mean photon count parameter ν_k is inversely proportional to its expected count [15],

$$F_k(\nu_k) = \frac{1}{\nu_k}. \tag{9}$$

The FI for the range parameter d can be found by reparametrization as

$$F_k(d) = \frac{1}{\nu_k}\left(\frac{\partial \nu_k}{\partial d}\right)^2 = \frac{\rho}{\sum_{i=c_k^l}^{c_k^u} \ell_i}\left(\sum_{i=c_k^l}^{c_k^u} \frac{10}{\log(10)}\alpha_i 10^{-\alpha_i d/10}(\varepsilon_i b_i(T_{\text{obj}}) - b_i(T_{\text{air}}))\right)^2. \tag{10}$$

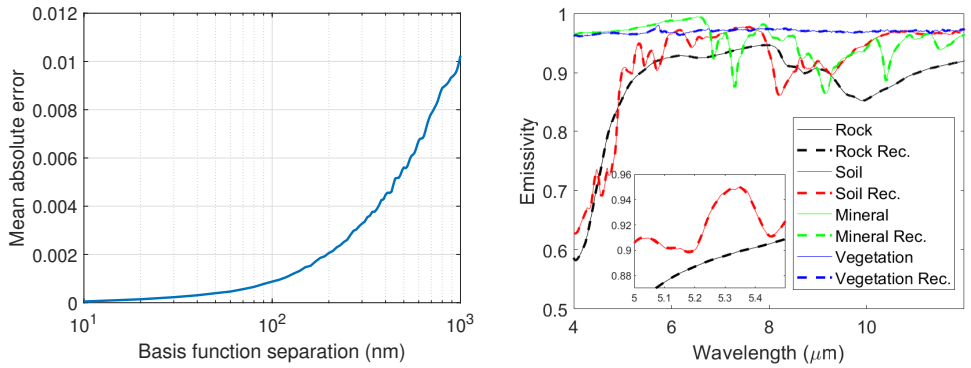

(a) MAE on ECOSTRESS emissivity database at various B-spline separations

(b) Projections of example emissivities

Fig. 1. Representation of emissivity profiles with B-spline basis functions (a) mean absolute error on ECOSTRESS Database at different B-spline separation, (b) projection of emisivity profiles onto space spanned by 50 nm-separated B-splines for several categories in the database: rock (*droite gneiss*), soil (*red-orange sandy soil*), mineral (*rivadavite*) and vegetation (*Abies concolor*). The inset shows a zoomed-in view of soil and mineral profiles.

The sensing model has many parameters. Among these, we assume that the air temperature, air pressure, and gas concentrations are known and can be used to calculate the atmospheric attenuation profile $\alpha(\lambda)$. With this knowledge, we seek to jointly estimate object temperature, emissivity, and range. The problem is still ill-posed since we measure radiance at K spectral channels for each element in the scene but have $K+2$ unknowns: the object's emissivity spectrum (of size K), temperature, and range. Therefore, there are many sets of parameters that could fit the same observed radiance and the Fisher information matrix becomes rank deficient.

The emissivity profiles of objects are typically smoother functions of wavelength than the absorption features of atmospheric gases [16–18]. We can exploit this to reduce the number of unknowns and hence make the problem well-posed. Specifically, we constrain the emissivity profile to be a linear combination of M smooth basis functions. With the basis functions stored in matrix $\mathbf{W} \in \mathbb{R}^{N\times M}$, we have

$$\boldsymbol{\varepsilon} = \mathbf{W}\mathbf{u} \tag{11}$$

for some coefficient vector $\mathbf{u} \in \mathbb{R}^M$. Inspired by [19], cubic B-splines are used to construct the basis functions. The separation between the B-spline knots is set to 50 nm, where a low residual error, 0.0004 mean absolute error shown in Fig. 1(a), is achieved on the ECOSTRESS spectral library [20, 21]. Fig. 1(b) shows example emissivities (solid) from ECOSTRESS and their projections (dashed). The projections can represent the emissivities with almost no error.

To calculate the FI with the object emission spectrum unknown, we define the matrix $\nabla\mathbf{I} \in \mathbb{R}^{K\times M+2}$ constructed by the partial derivatives of the measurements as

$$\nabla\mathbf{I} = \begin{bmatrix} \frac{\partial \nu_1}{\partial d} & \frac{\partial \nu_1}{\partial T_{\text{obj}}} & \frac{\partial \nu_1}{\partial u_1} & \frac{\partial \nu_1}{\partial u_2} & \cdots & \frac{\partial \nu_1}{\partial u_M} \\ \frac{\partial \nu_2}{\partial d} & \frac{\partial \nu_2}{\partial T_{\text{obj}}} & \frac{\partial \nu_2}{\partial u_1} & \frac{\partial \nu_2}{\partial u_2} & \cdots & \frac{\partial \nu_2}{\partial u_M} \\ \vdots & \vdots & \vdots & \vdots & \vdots & \vdots \\ \frac{\partial \nu_K}{\partial d} & \frac{\partial \nu_K}{\partial T_{\text{obj}}} & \frac{\partial \nu_K}{\partial u_1} & \frac{\partial \nu_K}{\partial u_2} & \cdots & \frac{\partial \nu_K}{\partial u_M} \end{bmatrix}, \tag{12}$$

where the partial derivatives are

$$\frac{\partial \nu_j}{\partial d} = \rho \sum_{i=c_j^l}^{c_j^u} -\frac{\log(10)}{10} \alpha_i 10^{-\alpha_i d/10} (\varepsilon_i b_i(T_{\text{obj}}) - b_i(T_{\text{air}})), \tag{13a}$$

$$\frac{\partial \nu_j}{\partial T_{\text{obj}}} = \rho \sum_{i=c_j^l}^{c_j^u} 10^{-\alpha_i d/10} \varepsilon_i \frac{\partial b_i(T_{\text{obj}})}{\partial T_{\text{obj}}}, \tag{13b}$$

$$\frac{\partial \nu_j}{\partial \varepsilon_i} = \begin{cases} \rho 10^{-\alpha_i d/10} b_i(T_{\text{obj}}), & \text{if } i \in [c_j^l, c_j^u]; \\ 0, & \text{otherwise,} \end{cases} \tag{13c}$$

$$\frac{\partial \boldsymbol{\nu}}{\partial \mathbf{u}} = \mathbf{W}^\intercal \frac{\partial \boldsymbol{\nu}}{\partial \boldsymbol{\varepsilon}}. \tag{13d}$$

Then using the noise model in Eq. (8), the Fisher information matrix $\mathbf{F}$ is given by

$$\mathbf{F} = \nabla \mathbf{I}^\top \text{diag}(1/\boldsymbol{\nu}) \nabla \mathbf{I}, \tag{14}$$

where $\text{diag}(1/\boldsymbol{\nu})$ is a diagonal matrix with an element-wise inverse of the mean photon count vector. Since the range parameter is the first element of our parameter vector, the CRB for its variance is the first diagonal element of the inverse of the Fisher information matrix:

$$\text{CRB}(d) = [\mathbf{F}^{-1}]_{1,1}. \tag{15}$$

4. Constrained Maximum Likelihood Estimator

Denoting the likelihood function that captures the shot-noise statistics in Eq. (8) as $f(\mathbf{y})$ and the emissivity constraint that was discussed in Section 3, the constrained maximum likelihood estimator MLE is

$$\begin{aligned} \widehat{d}, \widehat{T}, \widehat{\boldsymbol{\varepsilon}} = \underset{d,T,\boldsymbol{\varepsilon}}{\text{argmax}} \quad & f(\mathbf{y}|d,T,\boldsymbol{\varepsilon}) \\ \text{s.t.} \quad & \boldsymbol{\varepsilon} = \mathbf{W}\mathbf{u} \end{aligned} \tag{16}$$

where

$$f(\mathbf{y}|d,T,\boldsymbol{\varepsilon}) = \prod_{k=1}^{K} \frac{\nu_k(d,T,\boldsymbol{\varepsilon})^{y_k} e^{-\nu_k(d,T,\boldsymbol{\varepsilon})}}{y_k!}. \tag{17}$$

Taking the negative logarithm, the problem can be formulated as a minimization:

$$\begin{aligned} \widehat{d}, \widehat{T}, \widehat{\boldsymbol{\varepsilon}} = \underset{d,T,\boldsymbol{\varepsilon}}{\text{argmin}} \quad & \mathcal{L}(d,T,\boldsymbol{\varepsilon}) = -\sum_{k=1}^{K} y_k \log(\nu_k(d,T,\boldsymbol{\varepsilon})) - \nu_k(d,T,\boldsymbol{\varepsilon}) \\ \text{s.t.} \quad & \boldsymbol{\varepsilon} = \mathbf{W}\mathbf{u} \end{aligned} \tag{18}$$

We solve the optimization problem via projected gradient descent [22]. Expressions for the gradients can be computed using the chain rule, where the partial derivative of the loss function with respect to mean photon count is

$$\frac{\partial \mathcal{L}}{\partial \nu_i} = -\frac{y_i}{\nu_i} + 1, \tag{19}$$

and partial derivatives of mean photon count with respect to parameters of interest are given in Eq. (13).

5. Numerical Results

In Section 5.1, we discuss our atmospheric models including a standard atmosphere and three extreme-case atmospheres for simulations under a variety of conditions. In Section 5.2, we analyze the tradespace using the Fisher information at one wavelength to show how scene parameters affect the available range information, forming the building blocks of the later analysis. In Section 5.3, we analyze at which spectral bands the Fisher information is concentrated in the infrared spectrum. In Section 5.4, we analyze the CRB for range, including the sensor parameters and unknown object emission factors for performance analysis and compare it with the constrained MLE. In Section 5.5, we introduce read noise to our measurement model and illustrate its impact on ranging performance limits. Throughout Section 5 we assume unity detection efficiency at all wavelengths.

5.1. Atmospheric Models

The atmospheric models and corresponding attenuation profiles are computed using a high-resolution spectral modeling software package (SpectralCalc[1]) [13] that relies on the high-resolution transmission molecular absorption database (HITRAN) [23] with approximately 0.0198 nm sampling interval. To analyze the performance trends in a variety of situations, we used realistic atmospheric models built upon the US Standard atmospheric model [24]. We keep the pressure constant at 1013 hPa, and set the carbon dioxide volume mixing ratio (VMR) at 4.2×10^{-4} based on recent earth surface readings [25]. We vary the air temperature and water vapor concentration to capture the humidity variations in different situations. In particular, we analyze four different atmospheres with parameters listed in Table 1 and resulting attenuation functions depicted in Fig. 2. The air temperature changes from -50° C to 17° C, and to 50° C, in the range of the minimum ($\approx -89^\circ$ C) and maximum ($\approx 58^\circ$ C) air temperature recorded on earth, according to [26]. We calculate the maximum possible water vapor VMR level for a given air temperature and pressure based on [27], and vary the VMR levels from 6.9×10^{-5} to 5×10^{-2} carefully below the maximum VMR level. Increasing the water vapor concentration results in higher attenuation levels as there are more water vapor molecules to absorb and emit. Air temperature and pressure affect the width of individual absorption lines [11]; however, natural variations in surface air temperature and pressure have only small impacts on the attenuation profiles.

Table 1. Parameters used for the atmospheric models in the simulations; other parameters are kept the same as in the US standard atmosphere. The resulting attenuation profiles are shown in Fig. 2.

Parameter	Air Temperature	Water Vapor VMR	Relative Humidity
Cold	-50° C (223 K)	6.9×10^{-5}	97%
Standard	17° C (290 K)	1×10^{-2}	52%
Hot and Dry	50° C (323 K)	1×10^{-3}	0.77%
Hot and Humid	50° C (323 K)	5×10^{-2}	39%

5.2. Tradespace Analysis at One Wavelength

We use Fisher information analysis to show how scene parameters affect the range information. For this, we calculate the Fisher information with the finest resolution, the same resolution as that of the attenuation profiles in Section 5.1, to analyze the effect of scene parameters separately from

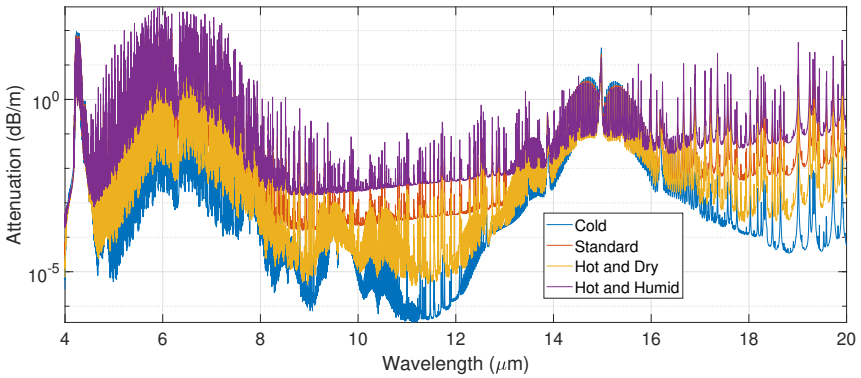

Fig. 2. Attenuation profiles of four atmospheric models used in the simulations. The water vapor concentration varies from a VMR of 6.9×10^{-5} to 5×10^{-2}, and the air temperature varies from -50° C (223 K) to 50° C (323 K). Carbon dioxide concentration is set to a VMR of 4.2×10^{-4} (equivalent to 420 ppm) based on recent readings [25]. Other parameters are kept the same as in the US Standard atmosphere detailed in [24].

sensor parameters. We show the Fisher information in Eq. (10), normalized by the scale factor ρ to achieve a single quantity for available information per $\mathrm{s} \cdot \mathrm{sr} \cdot \mathrm{cm}^2$ at a given wavelength, referred as Fisher information rate F_k/ρ. There are many scene parameters in Eq. (10) that affect the amount of information in the spectrum. We divide the scene parameters into two classes: the object-related parameters, including object temperature, object emissivity, and object range; and atmospheric parameters, including air temperature and attenuation coefficient.

Fig. 3 shows the Fisher information for the range parameter as a function of the temperature difference between the object and the air, and the object range. We use the Standard atmospheric model described in Table 1 for this analysis, but it can be generalized for other atmospheres as well. The temperature difference between the object and the air varies from -1 K to 3 K, and object range varies from 15 m to 2000 m. The *temperature contrast* $|\varepsilon_k b_k(T_{\mathrm{obj}}) - b_k(T_{\mathrm{air}})|$ is what matters in terms of range information. High contrast between the object emission and air black-body leads to more information. Note that we define the temperature contrast as the absolute radiance difference between the object emission and black-body at air temperature, which is different from temperature difference. As this contrast decreases, the Fisher information decreases and becomes zero at $\varepsilon_k b_k(T_{\mathrm{obj}}) = b_k(T_{\mathrm{air}})$. Depending on the object's emissivity, the object temperature that makes the Fisher information go to zero can change. More clearly, for high emissivity ($\varepsilon_k \approx 1$), this temperature is close to the air temperature, as shown in Fig. 3(a), but as the emissivity decreases, the object temperature that makes FI zero increases, as it is shown in Fig. 3(b). Note that the range information decays exponentially with the true object range, and closer objects yield more information.

Atmospheric parameters affect the range information mainly because they lead to a change in the attenuation coefficient and the black-body terms in Eq. (10). Fig. 4 shows the Fisher information as a function of attenuation and air temperature. The attenuation $\alpha \times d$ varies from 0 dB to 10 dB, while the air temperature varies from -50° C (223 K) to 50° C (323 K). The object is set to be vegetation (*Abies concolor*), located at 1000 m, and the temperature difference with respect to air is fixed at 5 K. The range information as a function of the attenuation coefficient includes a trade-off between too much attenuation and too little attenuation as can also be verified from Eq. (10). In the case of very low attenuation, the measurements are not sensitive to range, thus making the Fisher information approach zero. In contrast, for very high attenuation, light

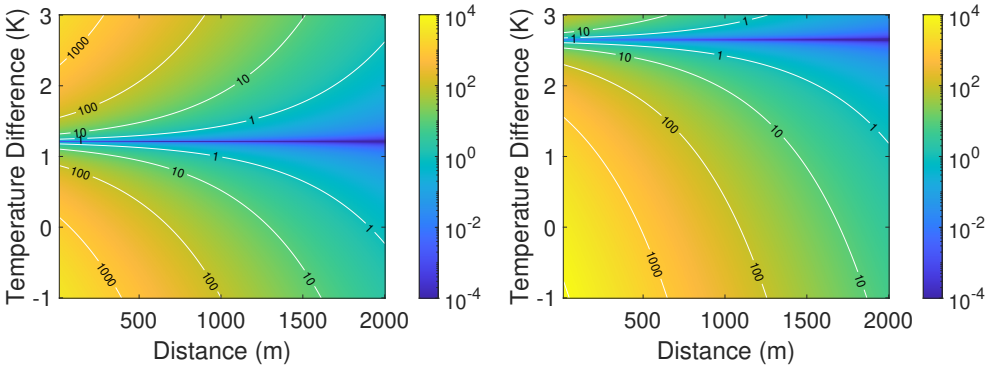

Fig. 3. Fisher information rate as a function of object parameters (temperature difference and range) at a fixed wavelength of 7.5 µm for (a) vegetation (*Abies concolor*), and (b) rock (*diorite gneiss*). The standard atmospheric model from Table 1 is used. The temperature difference between the object and the air varies from −1 K to +3 K. Object range varies from 15 m to 2000 m. The information increases as the temperature contrast $|\varepsilon_k b_k(T_{\text{obj}}) - b_k(T_{\text{air}})|$ increases. At $\varepsilon_k b_k(T_{\text{obj}}) = b_k(T_{\text{air}})$, the measurements are not sensitive to range, and the Fisher information is zero. Depending on the emissivity of the object this temperature can change. The Fisher information decays with $10^{-\alpha_k d/5}$ as the range increases.

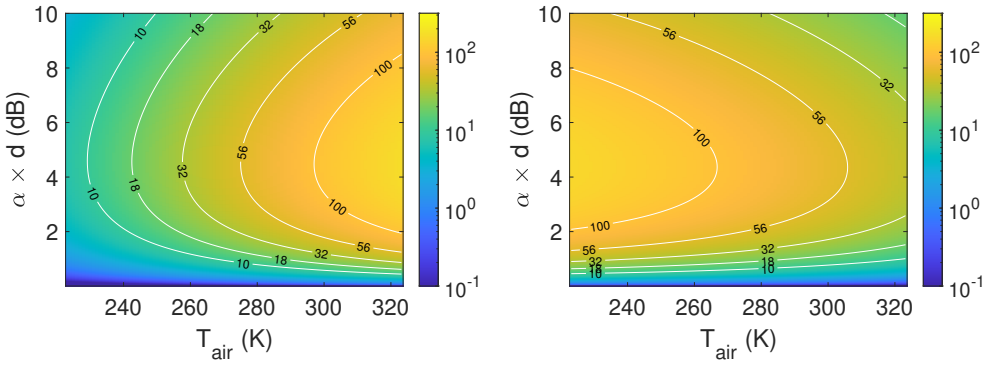

Fig. 4. Fisher information rate as a function of atmospheric parameters (air temperature and attenuation) at (a) 4 µm, and (b) 17 µm. The object emissivity is set to vegetation (*Abies concolor*) at 1000 m with constant 5 K temperature difference with respect to air. The air temperature varies from −50° C (223 K) to 50° C (323 K). The attenuation $\alpha \times d$ varies from 0 dB to 10 dB. Low attenuation, $\alpha \times d \approx 0$, results in low Fisher information because the measurements are not sensitive to range. For high attenuation, $\alpha \times d \to \infty$, the Fisher information decreases again because the object emission does not reach to the sensor. The optimal attenuation level that maximizes Eq. (10) is 4.3 dB. For fixed and small temperature differences, increasing air temperature increases the photon rate both for total count and black-body differences. Total counts increase the variance under shot noise and the black-body difference increases the Fisher information resulting in a trade-off that is wavelength dependent. Shorter wavelengths promotes high air temperature, whereas longer wavelengths promotes low air temperature.

from object emission does not reach the sensor and the Fisher information approaches zero. The optimal attenuation that maximizes Eq. (10) is given by $\alpha \times d = 4.3$ dB, which can be calculated with a gradient analysis [9]. Other than attenuation, the air temperature changes the amount of range information at a given band based on the black-body terms in Eq. (10). For a fixed and small temperature difference, both the temperature contrast $|\varepsilon_k b_k(T_{\text{obj}}) - b_k(T_{\text{air}})|$ and the total photon rates ν_k increase with air temperature. The temperature contrast increases the Fisher information shown in Fig. 3, whereas the higher photon rate increases the variance under shot noise, leading to a trade-off between these two terms. The trade-off for optimal air temperature is wavelength dependent as black-body terms are wavelength dependent. Shorter wavelengths tend to promote higher air temperatures, as shown in Fig. 4(a), whereas longer wavelengths tend to promote smaller air temperatures, as shown in Fig. 4(b).

5.3. Fisher Information in Infrared Spectrum

The atmospheric attenuation profile is sharp and encodes the range information at specific wavelengths in the spectrum. Each gas in the atmosphere has a spectral absorption signature that imposes specific shapes of range information based on the gas concentrations. At sea level, the spectral range under analysis, 4 µm to 20 µm, is dominated by carbon dioxide and water vapor. Carbon dioxide-dominated bands are around 4.15 µm to 4.45 µm and 14 µm to 16 µm, while water vapor is the main absorber for the rest of the spectrum.

Fig. 5 shows the Fisher information rate as a function of wavelength for different atmospheric models: (a) Cold; (b) Standard; (c) Hot and Dry; and (d) Hot and Humid. The resolution of each bin is set to 100 nm for visualization purposes. The object parameters are set to vegetation emissivity (*Abies concolor*), located at 10 m, 100 m, and 1000 m ranges, and exhibiting a 5 K relative temperature with respect to air. The spread of Fisher information depends on the range and the attenuation profile of the atmosphere. For short ranges, high water vapor VMR leads to more information overall. The most informative wavelengths are at the most absorptive wavelengths, around 4.15 µm to 4.45 µm, 5 µm to 8 µm, and 14 µm to 16 µm for all the models. As the range increases, the most informative wavelengths shift towards less absorptive wavelengths, depending on the VMR, because of the trade-off between too much absorption and too little absorption. For dry conditions, Fig. 5(a) and Fig. 5(c), the most informative bands tend to be in the same regions. In contrast, for humid conditions, Fig. 5(b) and Fig. 5(d), most informative bands shift towards less absorptive parts of the spectrum. Depending on the air temperature, some parts of the spectrum are promoted. For instance, for low air temperature longer wavelengths are more prominent, whereas for high air temperature shorter wavelengths are more prominent, which can be verified from Fig. 5(b) and Fig. 5(d).

Fig. 6 shows essential results and conclusions from the spread of the Fisher information in Fig. 5. For this analysis, we normalize the Fisher information rates with the total Fisher information rate in the spectrum $I_k(d)/\sum_{k=1}^{K} I_k(d)$, to compare the fractions of information coming from different spectral bands. Fig. 6(a) shows the fraction of total information from 4 µm to 5 µm, 5 µm to 8 µm, 8 µm to 13 µm, and 13 µm to 20 µm for the Standard atmospheric model. The bands between 4 µm to 5 µm and 8 µm to 13 µm are popular among many applications referred to as mid-wave infrared (MWIR) and long-wave infrared (LWIR) bands. On the contrary, the band between 5 µm to 8 µm is not that popular because many absorption lines corrupt the measurements if they are not handled carefully. For ranging in close range, where the optimal attenuation coefficient is high, 5 µm to 8 µm is the most valuable band. As the range increases, bands with lower attenuation levels increase their information fraction. The attenuation profile at the band between 8 µm to 13 µm is low compared to other parts of the spectrum analyzed. Nonetheless, for long ranges, around 1000 m to 2000 m, this band contains most of the information.

On the other hand, carbon dioxide is typically more homogeneous around the earth's atmosphere than water vapor. Therefore, it could be preferred when true gas concentration levels are not

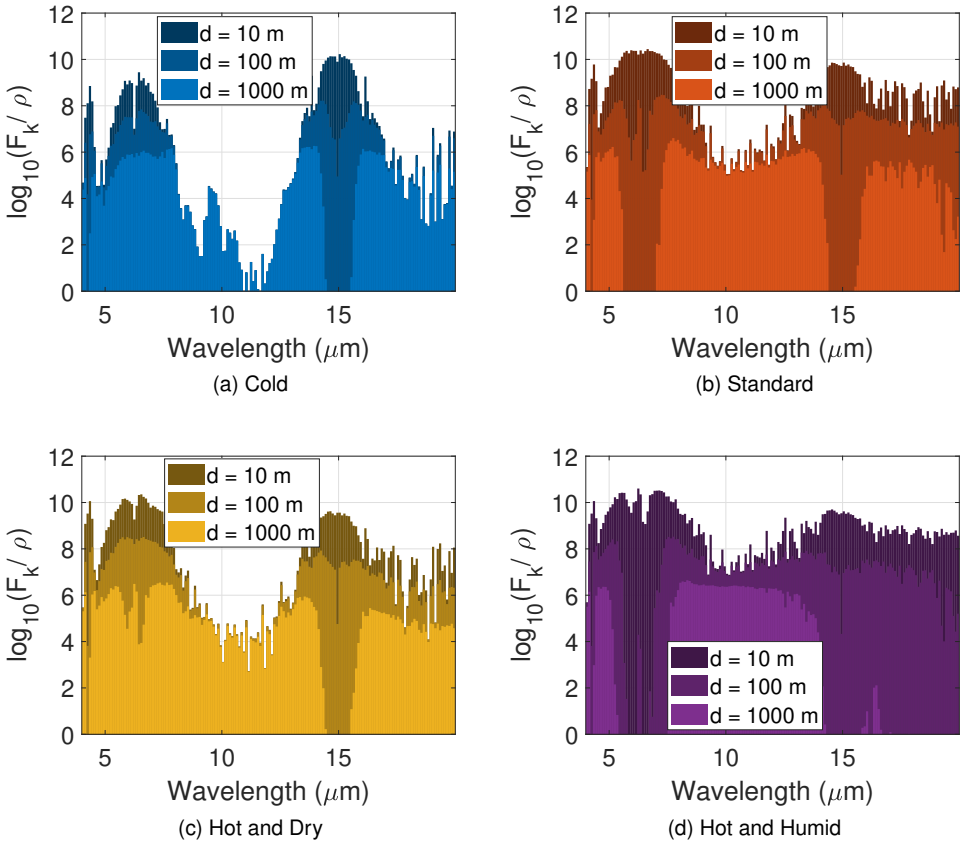

Fig. 5. Fisher information rate in log scale ($\log_{10}(F_k/\rho)$) for different atmospheric models: (a) Cold; (b) Standard; (c) Hot and Dry; and (d) Hot and Humid. The object is set to vegetation (*Abies concolor*) at 5 K relative temperature and 10 m, 100 m, and 1000 m ranges.

known. The negative side is that carbon dioxide-dominated bands only span a small portion of the full spectrum. Fig. 6(b) shows the fraction of range information from the carbon dioxide-dominated absorption bands. For the spectrum range analyzed here, the other fraction of range information is due to water vapor absorption. Carbon dioxide-dominated bands contain around 20% of the total information in the spectrum except for very cold atmospheric conditions. For dry conditions such as the Cold atmospheric model, in blue, carbon dioxide-dominated bands contain more information in close ranges as there is not enough attenuation from water vapor absorption lines. As the water vapor VMR increases, the fraction of information coming from water vapor increases, and conversely, the fraction from carbon dioxide bands decreases. Colder air also promotes the carbon dioxide band in longer wavelengths around 14 µm to 16 µm. Fig. 6(c) shows the cumulative Fisher information fraction after bands are sorted from most informative to least informative. Only a small portion of the full spectrum is informative about the range. For short ranges, after the 20% covered spectrum, we can cover around 90% of the total Fisher information. For longer ranges, around 1000 m, the information is more spread towards less attenuating bands, and more bands are required to approach the full amount of information.

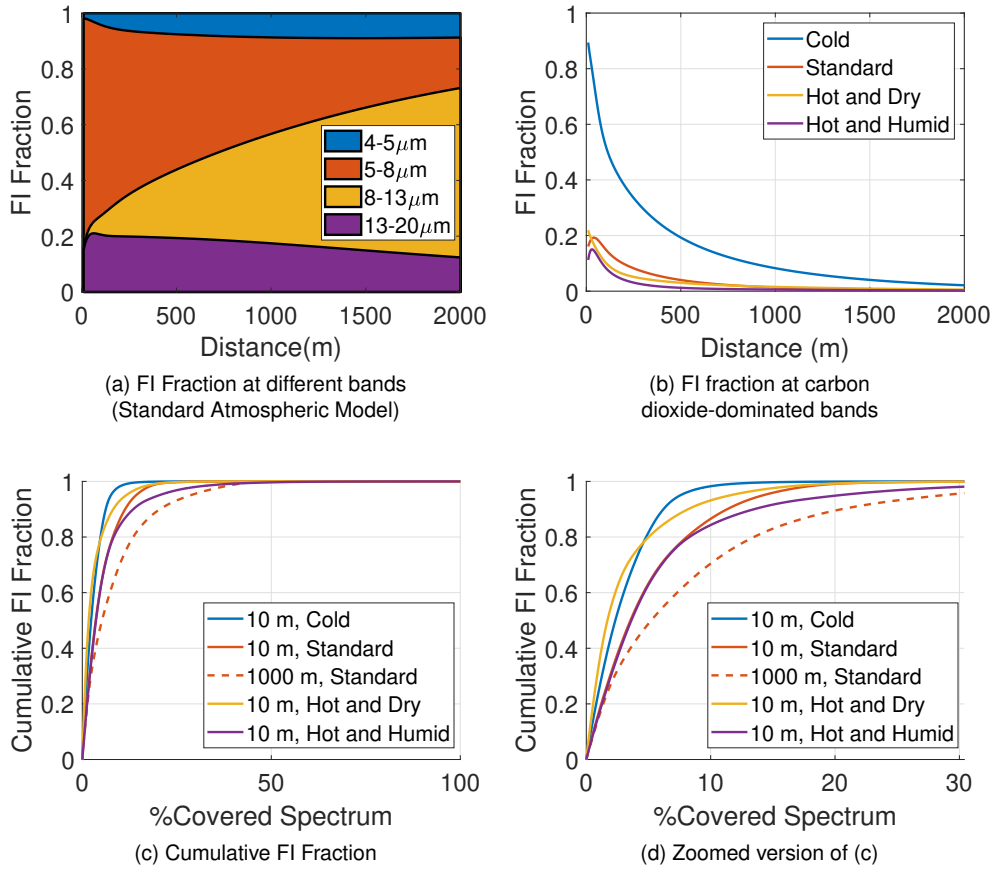

Fig. 6. Fraction of total Fisher information for (a) different bands at 4 µm–5 µm, 5 µm–8 µm, 8 µm–13 µm, and 13 µm–20 µm; (b) carbon dioxide-dominated bands at 4.15–4.45 µm and 14–16 µm; (c) and (d) cumulative Fisher information after sorting bands from most informative to least informative.

5.4. CRB Results

Using the CRB, we analyze the performance limits with unknown emissivities as a function of sensor parameters such as pixel size A (cm^2), solid angle Ω (sr), integration time t_d (s), and spectral resolution $\Delta\lambda$ (nm). We analyze an ideal shot noise-limited sensor with pixel size 100 µm^2, 2.9 f-number, and 250 µs integration time, and spectral resolution is varying from 0.1 nm to 100 nm. Fig. 7 shows simulations of CRB at different atmospheric models. The vertical axis is relative error, $\sqrt{CRB(d)}/d$. For the object, we use the vegetation emissivity profile (*Abies concolor*) at 5 K above the air temperature and at 10 m, 100 m, 1000 m range. For all of the conditions, spectral resolution follows a similar trend. Finer resolution improves the ranging accuracy. Between 0.1 nm to 10 nm resolution, the change is not very significant, and above 10 nm resolution the performance decays quickly. We note that the absorption line widths are approximately a few nanometers. For the other sensor parameters, the relative error is proportional with $1/\sqrt{\rho}$. Comparing the atmospheric conditions, the worst performance is expected in very cold environments, Fig. 7(a). Cold weather can hold less water vapor molecules [27], and are thus, not ideal for ranging especially for close ranges. Other atmospheric models show a very

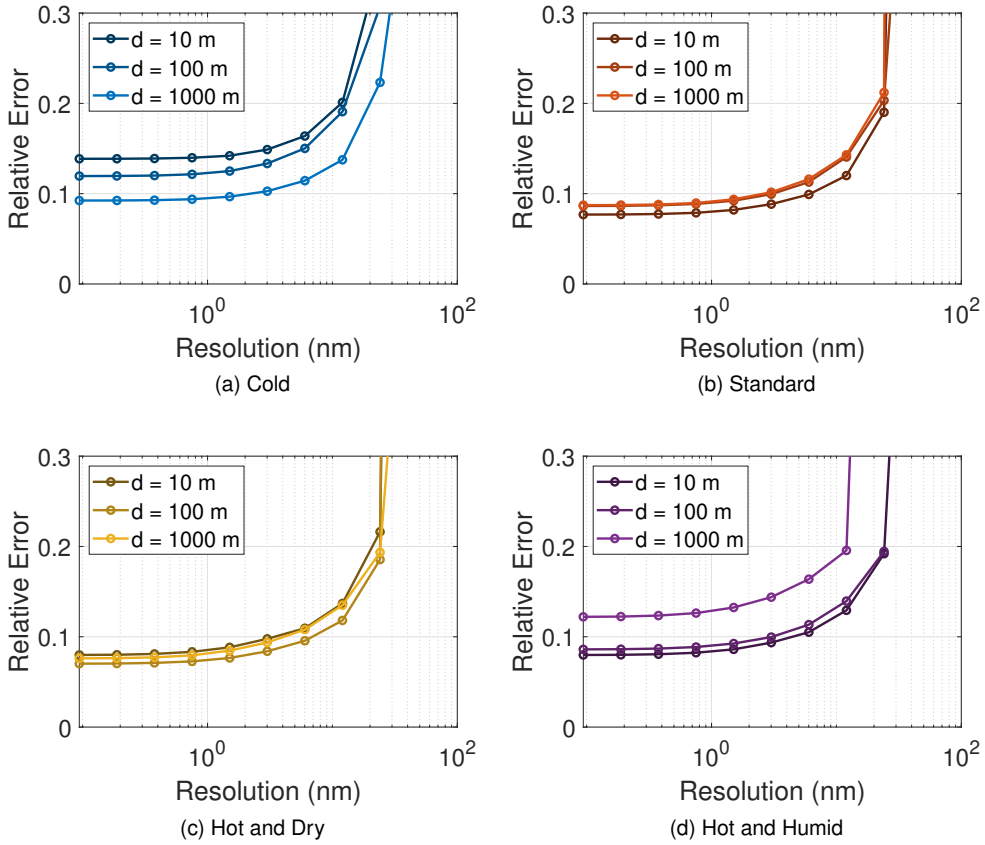

Fig. 7. CRB for different atmospheric models: (a) Cold; (b) Standard; (c) Hot and Dry; and (d) Hot and Humid. The sensor is simulated with pixel size 100 µm^2, 2.9 f-number, 250 µs integration time, and spectral resolution varying between 0.1 nm and 100 nm spanning 4 µm to 20 µm spectral range. The object is set to vegetation (*Abies concolor*) at 5 K relative temperature and 10 m, 100 m, and 1000 m ranges.

similar trend with small differences. For the Standard atmosphere Fig. 7(b), and the Hot and Dry atmospheric model Fig. 7(c), all ranges show a very similar performance curve. For Humid and Hot weather, Fig. 7(d), short ranges show the best relative error whereas long ranges of 1000 m and above are harder to resolve. This could be related to high attenuation levels due to high humidity, and the trade-off between too little attenuation and too much attenuation.

We analyze the performance of the MLE estimator in Fig. 8 comparing it with the CRB curve. For this analysis, we use the Standard atmosphere and the object is set to vegetation (*Abies concolor*) in blue, and mineral (*witherite*) in red. Both objects are set to 5 K above the air temperature and 100 m range. The sensor parameters are set to 100 µm^2 pixel size, 2.9 f-number, 250 µs integration time, and spectral resolution varying between 0.1 nm and 50 nm spanning the 7 µm to 9 µm spectral range. We used Monte Carlo simulations with 500 trials to calculate the MLE deviation. For fine channel resolution, we show that the maximum likelihood estimator performs near the CRB. As the channel resolution increases, it is harder to distinguish the sharp atmospheric effects from the smooth emission components. Approximately after 10 nm, the constrained MLE starts to deviate from the CRB. We analyze two emissivity profiles

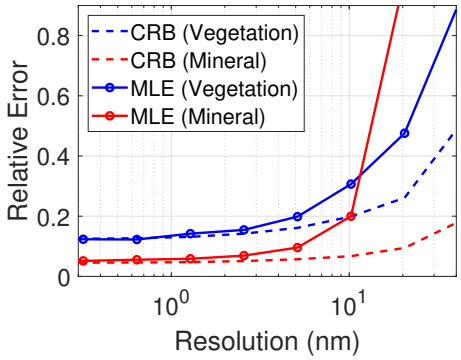

Fig. 8. CRB and MLE comparison for Standard atmospheric model. The sensor is simulated with pixel size 100 µm^2, 2.9 f-number, 250 µs integration time, and spectral resolution varying between 0.1 nm and 50 nm spanning 7 µm to 9 µm spectral range. The object is set to vegetation (*Abies concolor*) shown in blue and mineral (*witherite*) shown in red. Both objects are set to 5 K above air temperature and 100 m range. The relative error for MLE is calculated through Monte Carlo simulations with 500 trials.

to see possible mismatches due to representing emissivity profiles with lower dimensional representations. To analyze the worst-case scenario, we chose the emissivity profile with the largest residual error in the database, the mineral *witherite*. Even with the emissivities that show the largest residual error, the MLE performs near the CRB for fine spectral resolution. Note that although Fig. 8 predicts better performance for mineral than vegetation for these specific temperatures, results may vary for other temperature differences between objects and air, as shown in Fig. 3.

5.5. Effect of Read Noise

Our analysis to this point has neglected the effect of read noise and assumed shot noise-limited sensing. In this section, we discuss how read noise affects the CRB and show numerical results for different levels of read noise.

The read noise is typically modeled as additive Gaussian noise that is independent of the signal. For a read noise of σ^2, the probability distribution of the measurements from Eq. (8) can be modified to

$$y_k \sim \text{Poisson}(\nu_k) + \mathcal{N}(0, \sigma^2). \tag{20}$$

To yield a simple closed form for the Fisher information, we approximate the Poisson distribution as a normal distribution with matching mean and variance ν_k. Then the measurements follow a normal distribution,

$$y_k \sim \mathcal{N}(\nu_k, \nu_k + \sigma^2). \tag{21}$$

Following [28], the Fisher information for the parameter ν_k is

$$F_k(\nu_k) = \frac{1}{\nu_k + \sigma^2} + \frac{1}{2(\nu_k + \sigma^2)^2}. \tag{22}$$

Reparametrizing it for the parameters of interest results in the Fisher information matrix

$$\mathbf{F} = \nabla\mathbf{I}^\top \text{diag}(F_k(\nu_k))\nabla\mathbf{I}, \tag{23}$$

where the partial derivative matrix $\nabla\mathbf{I}$ is the same as in Eq. (12), and $\text{diag}(F_k(\nu_k))$ represents the diagonal matrix with entries F_k.

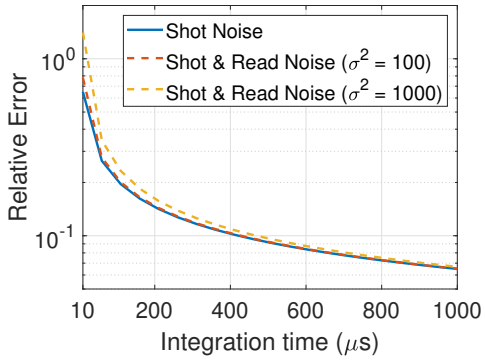

Fig. 9. CRB dependence on read noise. The solid blue curve is obtained with only shot noise. The dashed curves are obtained by including read noise as well, orange for 100 count and yellow for 1000 count read noise variance. The sensor is simulated with pixel size 100 µm^2, 2.9 f-number, 10 nm spectral resolution resolution spanning 4 µm to 20 µm spectral range, and integration time varying from 10 µs to 1000 µs. The Standard atmospheric model is used, and the object is chosen as vegetation (*Abies concolor*) at 100 m range and 5 K hotter than the air.

Fig. 9 shows the effect of read noise on CRB for 100 counts and 1000 counts of read noise, where the integration time varies from 10 µs to 1000 µs. The solid blue curve represents the CRB assuming only shot noise, and the dashed curves represent the CRB considering both shot noise and read noise, orange for 100 counts, and yellow for 1000 counts read noise variance. For shot noise alone, the relative error is inversely proportional to the square root of the integration time. Adding the read noise into the model leads to more uncertainty overall and causes a deviation from inverse proportionality with the square root of the integration time. For short integration times, the read noise plays the dominant factor as its variance is significantly higher than the shot noise. As the integration time grows, the dominant noise source switches to shot noise and the gap between considering and not considering read noise diminishes. For integration times around 100 µs, the shot noise ranges between $\approx$ 100 and $\approx$ 4500 counts per spectral channel and thus dominates over the read noise levels simulated here.

6. Conclusions

In this paper, we analyzed the performance and trade-offs of absorption-based ranging for a shot noise-limited sensing model. We presented a constrained MLE that accounts for the shot noise statistics of the measurements. As the problem is underdetermined, the prior distribution promoting smoothness for emissivity profile estimates is required for plausible range solutions. We presented the Fisher information and Cramer-Rao bound formulation for the range. The Fisher information has a closed-form solution that provides insights, and the CRB shows performance bounds as a function of the sensor parameters for ranging, accounting for unknown object emissivity and temperature.

We analyzed the effect of scene parameters on Fisher information at a given wavelength both for object-related and atmosphere-related parameters. For object-related parameters, the Fisher information is proportional to squared temperature contrast and decays exponentially with increasing range. For atmospheric parameters, both attenuation coefficient and air temperature have a trade-off. Low and high attenuation levels result in low Fisher information as both cases decrease the signal-to-noise ratio. The optimal attenuation level is at 4.3 dB, making the optimal attenuation coefficient range dependent as 4.3 dB$/d$. For fixed temperature differences, both

the total photon counts and photon counts attributed to temperature contrast increase with air temperature. The total number of photon counts increases the variance of the measurements, whereas the temperature contrast increases the sensitivity to range resulting in a trade-off. The optimal air temperature is wavelength dependent, for shorter wavelengths higher air temperatures increase the Fisher information, whereas for longer wavelengths lower air temperatures increase the Fisher information.

We analyze the spread of the Fisher information along the spectrum based on different atmospheric models such as Cold, Standard, Hot and Dry, and Hot and Humid. All of the atmospheric models showed a similar trend at short ranges, where the information is concentrated in the most absorptive bands, around 4.15 µm to 4.45 µm, 5 µm to 8 µm and 14 µm to 16 µm. Dry atmospheric models typically have lower attenuation profiles due to low levels of water vapor concentration, making it not ideal for short ranges. For long-range applications, dry weather can be useful as the optimal attenuation coefficient decreases. On the contrary, humid atmospheres have higher attenuation profiles ideal for short ranges but the information decays very quickly with increasing range. Cold weather promotes the longer wavelengths such as the carbon dioxide absorption region between 14 µm and 16 µm, whereas hot weather promotes shorter wavelengths such as the water vapor absorption region between 5 µm and 8 µm.

For the Standard atmosphere, most of the information is between 5 µm and 8 µm for short ranges. With increasing range, the 8 µm to 13 µm range contains the most Fisher information. There are two carbon dioxide-dominated absorption regions at 4.15 µm to 4.45 µm, and 14 µm to 16 µm which might be suitable for absorption-based ranging. One of the advantages of carbon dioxide is that it is well mixed in the atmosphere, much more homogeneously than water vapor. However, it is only a small portion of the full spectrum and usually covers less than 20% of the entire Fisher information, except in cold weather. For the Cold atmosphere, the water vapor content is so low that at short ranges most of the information comes from carbon dioxide-dominated absorption bands. As the information is concentrated in the absorption bands, some parts of the spectrum are not very useful. For short ranges, the Fisher information reaches 90% of the total information after 20% of the covered spectrum. The information is more spread at longer ranges and converges to full information after 40% of the covered spectrum.

We analyze the CRB including the unknown emissivity and object temperature for a shot noise-limited sensor with pixel size 100 µm^2, 2.9 f-number, and 250 µs integration time, and channel resolution varying from 0.1 nm to 100 nm. Finer resolution results in a lower relative error for every case. From 0.1 nm to 10 nm the change is not significant, obtaining around 10% relative error for every case. Some extreme cases such as very dry conditions at short ranges, and very humid conditions at longer ranges, have slightly worse performance. Above 10 nm resolution, the deviation quickly grows. For different parameters of the sensor, pixel size, solid angle, and integration time, the relative error is proportional to $1/\sqrt{\rho}$. Lastly, we validate the constrained maximum likelihood estimator that shows a close performance to the theoretical limit achieved by the CRB.

Funding. This work was supported in part by the US Defense Advanced Research Projects Agency (DARPA) Invisible Headlights program under contract number HR0011-20-S-0045 and in part by the US National Science Foundation under grant 1955219.

Disclosures. The authors declare no conflicts of interest.

Data Availability. Data underlying the results presented in this paper are not publicly available at this time but may be obtained from the authors upon reasonable request.

References

1. N. K. Leonpacher, "Passive infrared ranging," Master's thesis, Air Force Institute of Technology (1983).
2. M. R. Hawks, "Passive ranging using atmospheric oxygen absorption spectra," Ph.D. thesis, Air Force Institute of Technology (2006).

3. J. R. Anderson, "Monocular passive ranging by an optical system with band pass filtering," Master's thesis, Air Force Institute of Technology (2010).
4. Y. Nagase, T. Kushida, K. Tanaka, T. Funatomi, and Y. Mukaigawa, "Shape from thermal radiation: Passive ranging using multi-spectral LWIR measurements," in *Proceedings of the IEEE/CVF Conference on Computer Vision and Pattern Recognition,* (2022), pp. 12661–12671.
5. R. A. Vincent and M. R. Hawks, "Passive ranging of dynamic rocket plumes using infrared and visible oxygen attenuation," in *SPIE Acquisition, Tracking, Pointing, and Laser Systems Technologies XXV,* vol. 8052 (2011), p. 80520D.
6. D. J. Macdonald, M. R. Hawks, and K. C. Gross, "Passive ranging using mid-wavelength infrared atmospheric attenuation," in *SPIE Infrared Technology and Applications XXXVI,* vol. 7660 (2010), pp. 1269–1277.
7. J. R. Anderson, M. R. Hawks, K. C. Gross, and G. P. Perram, "Flight test of an imaging O_2(X-b) monocular passive ranging instrument," in *SPIE Airborne Intelligence, Surveillance, Reconnaissance (ISR) Systems and Applications VIII,* vol. 8020 (2011), pp. 38–49.
8. V. Cermak, L. Bodri, M. Kresl, P. Dedecek, and J. Safanda, "Eleven years of ground–air temperature tracking over different land cover types," Int. J. Climatol. **37**, 1084–1099 (2017).
9. U. D. Gallastegi, H. Rueda-Chacon, M. J. Stevens, and V. K. Goyal, "Absorption-based, passive range imaging from hyperspectral thermal measurements," arXiv e-Print 2308.05818 (2023).
10. U. D. Gallastegi, H. Rueda-Chacon, M. J. Stevens, and V. K. Goyal, "Absorption-based ranging from ambient thermal radiation without known emissivities," in *CLEO: Science and Innovations,* (2022), pp. STh5J–3.
11. D. G. Manolakis, R. B. Lockwood, and T. W. Cooley, *Hyperspectral Imaging Remote Sensing: Physics, Sensors, and Algorithms* (Cambridge University Press, 2016).
12. M. T. Eismann, *Hyperspectral Remote Sensing* (SPIE, 2012).
13. "Spectralcalc: High-resolution spectral modeling," https://www.spectralcalc.com. Accessed: 2022-06-05.
14. W. M. Elsasser, "Mean absorption and equivalent absorption coefficient of a band spectrum," Phys. Rev. **54**, 126 (1938).
15. M. J. Schervish and M. H. DeGroot, *Probability and Statistics*, vol. 563 (Pearson Education London, 2014).
16. D. Manolakis, M. Pieper, E. Truslow, R. Lockwood, A. Weisner, J. Jacobson, and T. Cooley, "Longwave infrared hyperspectral imaging: Principles, progress, and challenges," IEEE Geosci. Remote. Sens. Mag. **7**, 72–100 (2019).
17. C. C. Borel, "ARTEMISS – an algorithm to retrieve temperature and emissivity from hyper-spectral thermal image data," in *28th Annual GOMACTech Conference, Hyperspectral Imaging Session,* (2003).
18. C. Borel, "Error analysis for a temperature and emissivity retrieval algorithm for hyperspectral imaging data," Int. J. Remote. Sens. **29**, 5029–5045 (2008).
19. S. E. Golowich and D. G. Manolakis, "Cramer-Rao bounds for long-wave infrared gaseous plume quantification," Opt. Eng. **53**, 021109–021109 (2014).
20. S. K. Meerdink, S. J. Hook, D. A. Roberts, and E. A. Abbott, "The ECOSTRESS spectral library version 1.0," Remote. Sens. Environ. **230**, 111196 (2019).
21. A. Baldridge, S. Hook, C. Grove, and G. Rivera, "The ASTER spectral library version 2.0," Remote. Sens. Environ. **113**, 711–715 (2009).
22. N. Parikh and S. Boyd, "Proximal algorithms," Found. Trends Optim. **1**, 127–239 (2014).
23. I. E. Gordon *et al.*, "The HITRAN2020 molecular spectroscopic database," J. Quant. Spectrosc. Radiat. Transf. **277**, 107949 (2022).
24. National Oceanic and Atmospheric Administration, National Aeronautics and Space Adminsistration, and United States Air Force, *U.S. Standard Atmosphere, 1976* (U.S. Government Printing Office, 1976).
25. T. Stein, "Greenhouse gases continued to increase rapidly in 2022," (2023).
26. P. F. Krause and K. L. Flood, *Weather and Climate Extremes* (US Army Corps of Engineers, Topographic Engineering Center, 1997).
27. R. Stull, *Practical Meteorology: An Algebra-based Survey of Atmospheric Science*, BC Open Textbook Collection (AVP International, University of British Columbia, 2016).
28. M. Peng, J. Murray-Bruce, and V. K. Goyal, "Time-resolved focused ion beam microscopy: Modeling, estimation methods, and analyses," IEEE Trans. on Comput. Imaging **7**, 547–561 (2021).

Notes

[1]Certain commercial products or company names are identified here to describe our study adequately. Such identification is not intended to imply recommendation or endorsement by the National Institute of Standards and Technology, nor is it intended to imply that the products or names identified are necessarily the best available.